EUROPEAN ORGANISATION FOR NUCLEAR RESEARCH

CERN-EP/2003-023
5th May 2003

# Measurement of Isolated Prompt Photon Production in Photon-Photon Collisions at $\sqrt{s_{ee}} = 183 - 209$ GeV

The OPAL Collaboration

Abstract

For the first time at LEP the production of prompt photons is studied in the collisions of quasi-real photons using the OPAL data taken at $e^+e^-$ centre-of-mass energies between 183 GeV and 209 GeV. The total inclusive production cross-section for isolated prompt photons in the kinematic range of transverse momentum $p_T^\gamma > 3.0$ GeV and pseudorapidity $|\eta^\gamma| < 1$ is determined to be $\sigma_{tot} = 0.32 \pm 0.04$ (stat) $\pm 0.04$ (sys) pb. Differential cross-sections are compared to the predictions of a next-to-leading-order (NLO) calculation.

(To be submitted to Eur. Phys. J. C)

# The OPAL Collaboration


G. Abbiendi[2], C. Ainsley[5], P.F. Åkesson[3], G. Alexander[22], J. Allison[16], P. Amaral[9], G. Anagnostou[1], K.J. Anderson[9], S. Arcelli[2], S. Asai[23], D. Axen[27], G. Azuelos[18,a], I. Bailey[26], E. Barberio[8,p], R.J. Barlow[16], R.J. Batley[5], P. Bechtle[25], T. Behnke[25], K.W. Bell[20], P.J. Bell[1], G. Bella[22], A. Bellerive[6], G. Benelli[4], S. Bethke[32], O. Biebel[31], O. Boeriu[10], P. Bock[11], M. Boutemeur[31], S. Braibant[8], L. Brigliadori[2], R.M. Brown[20], K. Buesser[25], H.J. Burckhart[8], S. Campana[4], R.K. Carnegie[6], B. Caron[28], A.A. Carter[13], J.R. Carter[5], C.Y. Chang[17], D.G. Charlton[1], A. Csilling[29], M. Cuffiani[2], S. Dado[21], A. De Roeck[8], E.A. De Wolf[8,s], K. Desch[25], B. Dienes[30], M. Donkers[6], J. Dubbert[31], E. Duchovni[24], G. Duckeck[31], I.P. Duerdoth[16], E. Etzion[22], F. Fabbri[2], L. Feld[10], P. Ferrari[8], F. Fiedler[31], I. Fleck[10], M. Ford[5], A. Frey[8], A. Fürtjes[8], P. Gagnon[12], J.W. Gary[4], G. Gaycken[25], C. Geich-Gimbel[3], G. Giacomelli[2], P. Giacomelli[2], M. Giunta[4], J. Goldberg[21], E. Gross[24], J. Grunhaus[22], M. Gruwé[8], P.O. Günther[3], A. Gupta[9], C. Hajdu[29], M. Hamann[25], G.G. Hanson[4], K. Harder[25], A. Harel[21], M. Harin-Dirac[4], M. Hauschild[8], C.M. Hawkes[1], R. Hawkings[8], R.J. Hemingway[6], C. Hensel[25], G. Herten[10], R.D. Heuer[25], J.C. Hill[5], K. Hoffman[9], D. Horváth[29,c], P. Igo-Kemenes[11], K. Ishii[23], H. Jeremie[18], P. Jovanovic[1], T.R. Junk[6], N. Kanaya[26], J. Kanzaki[23,u], G. Karapetian[18], D. Karlen[26], K. Kawagoe[23], T. Kawamoto[23], R.K. Keeler[26], R.G. Kellogg[17], B.W. Kennedy[20], D.H. Kim[19], K. Klein[11,t], A. Klier[24], S. Kluth[32], T. Kobayashi[23], M. Kobel[3], S. Komamiya[23], L. Kormos[26], T. Krämer[25], P. Krieger[6,l], J. von Krogh[11], K. Kruger[8], T. Kuhl[25], M. Kupper[24], G.D. Lafferty[16], H. Landsman[21], D. Lanske[14], J.G. Layter[4], A. Leins[31], D. Lellouch[24], J. Letts[o], L. Levinson[24], J. Lillich[10], S.L. Lloyd[13], F.K. Loebinger[16], J. Lu[27,w], J. Ludwig[10], A. Macpherson[28,i], W. Mader[3], S. Marcellini[2], A.J. Martin[13], G. Masetti[2], T. Mashimo[23], P. Mättig[m], W.J. McDonald[28], J. McKenna[27], T.J. McMahon[1], R.A. McPherson[26], F. Meijers[8], W. Menges[25], F.S. Merritt[9], H. Mes[6,a], A. Michelini[2], S. Mihara[23], G. Mikenberg[24], D.J. Miller[15], S. Moed[21], W. Mohr[10], T. Mori[23], A. Mutter[10], K. Nagai[13], I. Nakamura[23,V], H. Nanjo[23], H.A. Neal[33], R. Nisius[32], S.W. O'Neale[1], A. Oh[8], A. Okpara[11], M.J. Oreglia[9], S. Orito[23,*], C. Pahl[32], G. Pásztor[4,g], J.R. Pater[16], G.N. Patrick[20], J.E. Pilcher[9], J. Pinfold[28], D.E. Plane[8], B. Poli[2], J. Polok[8], O. Pooth[14], M. Przybycień[8,n], A. Quadt[3], K. Rabbertz[8,r], C. Rembser[8], P. Renkel[24], J.M. Roney[26], S. Rosati[3], Y. Rozen[21], K. Runge[10], K. Sachs[6], T. Saeki[23], E.K.G. Sarkisyan[8,j], A.D. Schaile[31], O. Schaile[31], P. Scharff-Hansen[8], J. Schieck[32], T. Schörner-Sadenius[8], M. Schröder[8], M. Schumacher[3], C. Schwick[8], W.G. Scott[20], R. Seuster[14,f], T.G. Shears[8,h], B.C. Shen[4], P. Sherwood[15], G. Siroli[2], A. Skuja[17], A.M. Smith[8], R. Sobie[26], S. Söldner-Rembold[16,d], F. Spano[9], A. Stahl[3], K. Stephens[16], D. Strom[19], R. Ströhmer[31], S. Tarem[21], M. Tasevsky[8], R.J. Taylor[15], R. Teuscher[9], M.A. Thomson[5], E. Torrence[19], D. Toya[23], P. Tran[4], I. Trigger[8], Z. Trócsányi[30,e], E. Tsur[22], M.F. Turner-Watson[1], I. Ueda[23], B. Ujvári[30,e], C.F. Vollmer[31], P. Vannerem[10], R. Vértesi[30], M. Verzocchi[17], H. Voss[8,q], J. Vossebeld[8,h], D. Waller[6], C.P. Ward[5], D.R. Ward[5], P.M. Watkins[1], A.T. Watson[1], N.K. Watson[1], P.S. Wells[8], T. Wengler[8], N. Wermes[3], D. Wetterling[11] G.W. Wilson[16,k], J.A. Wilson[1], G. Wolf[24], T.R. Wyatt[16], S. Yamashita[23], D. Zer-Zion[4], L. Zivkovic[24]

[1]School of Physics and Astronomy, University of Birmingham, Birmingham B15 2TT, UK
[2]Dipartimento di Fisica dell' Università di Bologna and INFN, I-40126 Bologna, Italy
[3]Physikalisches Institut, Universität Bonn, D-53115 Bonn, Germany

[4]Department of Physics, University of California, Riverside CA 92521, USA
[5]Cavendish Laboratory, Cambridge CB3 0HE, UK
[6]Ottawa-Carleton Institute for Physics, Department of Physics, Carleton University, Ottawa, Ontario K1S 5B6, Canada
[8]CERN, European Organisation for Nuclear Research, CH-1211 Geneva 23, Switzerland
[9]Enrico Fermi Institute and Department of Physics, University of Chicago, Chicago IL 60637, USA
[10]Fakultät für Physik, Albert-Ludwigs-Universität Freiburg, D-79104 Freiburg, Germany
[11]Physikalisches Institut, Universität Heidelberg, D-69120 Heidelberg, Germany
[12]Indiana University, Department of Physics, Bloomington IN 47405, USA
[13]Queen Mary and Westfield College, University of London, London E1 4NS, UK
[14]Technische Hochschule Aachen, III Physikalisches Institut, Sommerfeldstrasse 26-28, D-52056 Aachen, Germany
[15]University College London, London WC1E 6BT, UK
[16]Department of Physics, Schuster Laboratory, The University, Manchester M13 9PL, UK
[17]Department of Physics, University of Maryland, College Park, MD 20742, USA
[18]Laboratoire de Physique Nucléaire, Université de Montréal, Montréal, Québec H3C 3J7, Canada
[19]University of Oregon, Department of Physics, Eugene OR 97403, USA
[20]CLRC Rutherford Appleton Laboratory, Chilton, Didcot, Oxfordshire OX11 0QX, UK
[21]Department of Physics, Technion-Israel Institute of Technology, Haifa 32000, Israel
[22]Department of Physics and Astronomy, Tel Aviv University, Tel Aviv 69978, Israel
[23]International Centre for Elementary Particle Physics and Department of Physics, University of Tokyo, Tokyo 113-0033, and Kobe University, Kobe 657-8501, Japan
[24]Particle Physics Department, Weizmann Institute of Science, Rehovot 76100, Israel
[25]Universität Hamburg/DESY, Institut für Experimentalphysik, Notkestrasse 85, D-22607 Hamburg, Germany
[26]University of Victoria, Department of Physics, P O Box 3055, Victoria BC V8W 3P6, Canada
[27]University of British Columbia, Department of Physics, Vancouver BC V6T 1Z1, Canada
[28]University of Alberta, Department of Physics, Edmonton AB T6G 2J1, Canada
[29]Research Institute for Particle and Nuclear Physics, H-1525 Budapest, P O Box 49, Hungary
[30]Institute of Nuclear Research, H-4001 Debrecen, P O Box 51, Hungary
[31]Ludwig-Maximilians-Universität München, Sektion Physik, Am Coulombwall 1, D-85748 Garching, Germany
[32]Max-Planck-Institute für Physik, Föhringer Ring 6, D-80805 München, Germany
[33]Yale University, Department of Physics, New Haven, CT 06520, USA

[a] and at TRIUMF, Vancouver, Canada V6T 2A3
[c] and Institute of Nuclear Research, Debrecen, Hungary
[d] and Heisenberg Fellow
[e] and Department of Experimental Physics, Lajos Kossuth University, Debrecen, Hungary
[f] and MPI München
[g] and Research Institute for Particle and Nuclear Physics, Budapest, Hungary
[h] now at University of Liverpool, Dept of Physics, Liverpool L69 3BX, U.K.
[i] and CERN, EP Div, 1211 Geneva 23
[j] and Manchester University
[k] now at University of Kansas, Dept of Physics and Astronomy, Lawrence, KS 66045, U.S.A.

[l] now at University of Toronto, Dept of Physics, Toronto, Canada
[m] current address Bergische Universität, Wuppertal, Germany
[n] now at University of Mining and Metallurgy, Cracow, Poland
[o] now at University of California, San Diego, U.S.A.
[p] now at Physics Dept Southern Methodist University, Dallas, TX 75275, U.S.A.
[q] now at IPHE Université de Lausanne, CH-1015 Lausanne, Switzerland
[r] now at IEKP Universität Karlsruhe, Germany
[s] now at Universitaire Instelling Antwerpen, Physics Department, B-2610 Antwerpen, Belgium
[t] now at RWTH Aachen, Germany
[u] and High Energy Accelerator Research Organisation (KEK), Tsukuba, Ibaraki, Japan
[v] now at University of Pennsylvania, Philadelphia, Pennsylvania, USA
[w] now at TRIUMF, Vancouver, Canada
[*] Deceased

# 1 Introduction

We present the first LEP measurement of the inclusive production of isolated prompt photons in photon-photon collisions, $\gamma\gamma \to \gamma + \mathrm{X}$, where X denotes the hadronic final state produced in addition to the photon. The interacting photons are emitted by the beam electrons[1]. Electrons scattered at small angles into the beam pipe escape detection and, in this analysis, events with one or two detected scattered electrons are vetoed ("anti-tagging"). The interacting photons thus carry a small four-momentum squared, $Q^2$, i.e. they are quasi-real.

In leading order (LO), only processes where one ("single-resolved") or both ("double-resolved") of the incoming photons fluctuate into a hadronic state contribute to the production cross-section for prompt photons. In these processes, a quark or a gluon from the hadronic state participates in the hard interaction, $\mathrm{q}\gamma \to \mathrm{q}\gamma$ (Fig. 1), $\mathrm{q}\overline{\mathrm{q}} \to \gamma\mathrm{g}$ and $\mathrm{g}\gamma \to \mathrm{q}\gamma$ (Fig. 2). Processes with final state radiation ("FSR") are a higher-order contribution to the direct process (Fig. 3).

The hadronic structure of the photon has previously been studied by OPAL in the interactions of two quasi-real photons producing jets [1], hadrons [2] or $\mathrm{D}^*$ mesons [3] at high transverse momentum. The inclusive production cross-section for isolated prompt photons is expected to be about two orders of magnitude smaller than for di-jet production in a similar kinematic region of transverse energy $E_{\mathrm{T}} > 3$ GeV and pseudorapidity $|\eta| < 1$ [1]. Hadronisation uncertainties, however, are expected to be much smaller than in the case of jet production at similar transverse momenta, allowing a complementary study of the hadronic structure of photon interactions [4, 5]. The photoproduction of prompt photons has previously been studied by NA14 [6] and by ZEUS [7].

Approximately 649 $\mathrm{pb}^{-1}$ of $\mathrm{e}^+\mathrm{e}^-$ collision data taken by the OPAL experiment at centre-of-mass energies $\sqrt{s_{\mathrm{ee}}}$ from 183 GeV to 209 GeV are used in this analysis. Since the expected production cross-section is small and the increase of the cross-section from the lowest to the highest centre-of-mass energy is expected to be less than the statistical uncertainty of the

[1] Positrons are also referred to as electrons.

measurement [4], all data are combined for the final result. The luminosity-weighted mean $e^+e^-$ centre-of-mass energy is approximately 196.6 GeV. The measured differential and total cross-sections are compared to the leading order predictions of the Monte Carlo generator PYTHIA [8] and to a next-to-leading-order (NLO) calculation [9]. The measurement is restricted to isolated prompt photons to suppress background from neutral particle decays into photons.

# 2 The OPAL detector

A detailed description of the OPAL detector can be found in [10], and therefore only a brief account of the main features relevant to the present analysis will be given here.

The central tracking system is located inside a solenoidal magnet which provides a uniform axial magnetic field of 0.435 T. The magnet is surrounded by a lead-glass electromagnetic calorimeter (ECAL) and a hadronic sampling calorimeter (HCAL). The HCAL is surrounded by muon chambers. There are similar layers of detectors in the endcaps. The region around the beam pipe on both sides of the detector is covered by the forward calorimeters and the silicon-tungsten luminometers.

Starting with the innermost components, the tracking system consists of a high precision silicon microvertex detector (SI), a precision vertex drift chamber (CV), a large volume jet chamber (CJ) with 159 layers of axial anode wires and a set of $z$ chambers measuring the track coordinates along the beam direction[2].

The ECAL covers the complete azimuthal range for polar angles satisfying $|\cos\theta| < 0.98$. The barrel section, which covers the polar angle range $|\cos\theta| < 0.82$, consists of a cylindrical array of 9440 lead-glass blocks with a depth of 24.6 radiation lengths. Each block subtends an angular region of approximately $40 \times 40$ mrad$^2$. Deposits of energy in adjacent blocks are grouped together to form clusters. The intrinsic energy resolution of $\sigma_E/E = 0.2\% \oplus 6.3\%/\sqrt{E}$ is substantially degraded (by a factor $\simeq 2$) due to the presence of at least two radiation lengths of material in front of the lead glass.

The endcap sections consist of 1132 lead-glass blocks with a depth of more than 22 radiation lengths, covering the range of polar angles between $0.81 < |\cos\theta| < 0.98$. The HCAL consists of streamer tubes and thin multiwire chambers instrumenting the gaps in the iron yoke of the magnet, which provides the absorber material of 4 or more interaction lengths.

Scintillators in the barrel and endcap regions provide time measurements for the large fraction of photons which convert in the material in front of the ECAL. They are also used to reject the background from cosmic ray interactions. The barrel time-of-flight (TOF) scintillator bars are located outside the solenoid in front of the barrel ECAL and match its geometrical acceptance ($|\cos\theta| < 0.82$).

The forward calorimeters (FD) at each end of the OPAL detector consist of cylindrical lead-

[2]In the OPAL coordinate system the $x$ axis points towards the centre of the LEP ring, the $y$ axis points upwards and the $z$ axis points in the direction of the electron beam. The polar angle $\theta$ is defined with respect to the $z$ axis. The azimuthal angle $\phi$ and the radius $r$ denote the usual spherical coordinates.

scintillator calorimeters with a depth of 24 radiation lengths. The acceptance of the forward calorimeters covers the angular range from 47 to 140 mrad from the beam direction. The silicon tungsten detectors (SW) [11] at each end of the OPAL detector cover the angular region between 25 mrad and 59 mrad in front of the forward calorimeters. Due to a radiation shield installed for LEP2 running, the lower edge of the useful acceptance is 33 mrad. Each calorimeter consists of 19 layers of silicon detectors and 18 layers of tungsten, corresponding to a total of 22 radiation lengths.

# 3 Process kinematics and Monte Carlo simulation

The kinematic properties of the two interacting photons are described by their negative squared four-momentum transfers, $Q^2_{i=1,2}$, which are related to the scattering angles $\theta'_i$ of the corresponding electron relative to the beam direction by

$$Q_i^2 = -(k_i - k_i')^2 \approx 2E_iE_i'(1 - \cos\theta_i'), \tag{1}$$

neglecting the mass $m_\mathrm{e}$ of the electron. The quantities $k_i$ and $k'_i$ are the four-momenta of the beam and scattered electrons, and $E_i$ and $E'_i$ their energies. The maximum squared four-momentum transfer, $Q^2_{\mathrm{max}}$, is given by Eq. 1 using the limits on the energy and the polar angle from the anti-tagging requirement that no electron has been detected in the ECAL, FD or SW calorimeters. These cuts correspond to $Q^2_{\mathrm{max}} \approx 10$ GeV$^2$. No correction for this anti-tagging condition is applied. The median $Q^2$ resulting from this definition cannot be determined with the data since the scattered electrons are not tagged. For the kinematic range of this analysis the Monte Carlo simulations predict the median $Q^2$ to be of the order $10^{-4}$ GeV$^2$.

The Monte Carlo generator PYTHIA 6.130 [8] is used for the simulation of signal events, $\gamma\gamma \to \gamma$+X. Separate samples of single and double-resolved processes have been produced using the SaS-1D [12], GRV-LO [13], and LAC-1 [14] parametrisations of the parton distributions of the photon. The samples are generated at $\mathrm{e^+e^-}$ centre-of-mass energies $\sqrt{s_{\mathrm{ee}}}$ of 189 GeV, 192 GeV, and 206 GeV.

Several samples are generated for systematic studies: single-resolved signal events with HERWIG [15] and signal events with final state photon radiation with PHOJET 1.10 [16] using the parton shower option of JETSET [8]. Photon-photon events with initial state photon radiation are simulated using BDK [17].

The transition from quasi-real to virtual photons is smooth and the definition used to separate these kinematic regions is somewhat arbitrary. In the Monte Carlo simulation we choose values of $Q^2 < 4.5$ GeV$^2$ to define quasi-real photons. The background from hadronic $\gamma\gamma$ events without prompt photon production is simulated with PHOJET for the case where both photons have $Q^2 < 4.5$ GeV$^2$. In PHOJET the fragmentation into hadrons is performed using JETSET. HERWIG 5.9 is used to simulate $\gamma\gamma$ events where one photon has $Q^2 < 4.5$ GeV$^2$ and the other photon has $Q^2 > 4.5$ GeV$^2$. This combination of generators gives a good description of hadronic two-photon events [1]. Two-photon events with fully leptonic final states are simulated with Vermaseren 1.0 [18].

PYTHIA 5.7 and KK2f [19] are used for the description of $q\overline{q}(\gamma)$ events produced in $e^+e^-$ annihilations. KORALZ 4.02 [20] and KK2f are used to simulate $\tau$ pairs. Four-fermion final states are simulated with grc4f 2.1 [21] and KORALW [22].

A photon signal in the electromagnetic calorimeter can originate from a prompt photon but also from $\pi^0$ or $\eta$ mesons decaying into two photons. Background is also expected from the annihilation of antineutrons, $\bar{n}$, in the detector material. The different distributions of energy deposited in the calorimeter for signal and background can be used to separate signal from background by a cluster shape analysis. To study the response of the electromagnetic calorimeter to the various sources of background, Monte Carlo samples are generated using a single-particle generator. These particles are generated with a flat $p_T$ distribution in the range of 2 GeV to 13 GeV, and flat azimuthal angle $\phi$ and flat pseudorapidity $\eta = -\ln(\tan(\theta/2))$ distributions over the acceptance of the barrel part of the detector. Exponential $p_T$-dependent weighting functions are introduced to reproduce the shape of the $p_T$ distributions as predicted by PHOJET.

All Monte Carlo samples are passed through a full simulation of the OPAL detector [23] and are analysed using the same reconstruction algorithms as for data.

# 4 Event selection

Only anti-tagged photon-photon scattering events are studied in this analysis. The same event selection is applied to the data samples taken at different $e^+e^-$ centre-of-mass energies $\sqrt{s_{ee}}$. Anti-tagged photon-photon events are selected using the following requirements:

- Anti-tagged events are selected by vetoing all events containing an energy deposit of more than 15% of $\sqrt{s_{ee}}$ in the SW calorimeter or more than 25% of $\sqrt{s_{ee}}$ in the FD calorimeter, in either hemisphere of the detector. This corresponds to a maximum allowed scattering angle of the beam electrons of $\theta' = 33$ mrad for electrons with energies above the threshold.

- At least three tracks must be found in the tracking chambers. A track is required to have a minimum transverse momentum of 120 MeV and more than 20 hits in the central jet chamber. In this paper, transverse is always defined with respect to the $z$ direction of the detector. The distance of closest approach to the origin must be less than 20 cm in the $z$ direction and less than 2.5 cm in the $r\phi$ plane. An event is rejected if a track with a momentum higher than 25% of the centre-of-mass energy is detected.

- A minimum visible invariant mass of the event, $W_{vis}$, of more than 5 GeV is required. To reduce the $e^+e^-$ annihilation background, $W_{vis}$ should be less than 30% of $\sqrt{s_{ee}}$. $W_{vis}$ is calculated using the energies and positions of clusters measured in the ECAL, HCAL, FD and SW calorimeters and using the momenta of tracks. A matching algorithm [24] is applied to compensate for double-counting of particle momenta in the calorimeters and in the tracking chambers.

- The background due to beam-gas or beam-wall interactions is reduced by requiring the absolute value of the net charge of an event, calculated by adding the charges of the

tracks, to be less than three. In addition, the ratio of the longitudinal component of the momentum vector of the final state to the total visible energy is required to be smaller than 0.98.

Photon candidates are selected as follows:

- The photon candidates are reconstructed using the same algorithm as in [25]. Only clusters in the ECAL which consist of at least 2 lead-glass blocks and fewer than 13 blocks are taken. If a track is associated with the cluster, the candidate is rejected. The cluster has to be totally contained in the barrel part of the calorimeter; clusters with blocks in the end cap calorimeter are rejected. The pseudorapidity of the photon, $\eta^\gamma$, is required to be in the range $-1 < \eta^\gamma < 1$. The minimum transverse momentum of the photon candidate with respect to the beam axis, $p_{\mathrm{T}}^\gamma$, is 3 GeV. The energy $E_\gamma$ and the polar angle $\theta_\gamma$ of the photon candidate are calculated from the energy and position of the cluster.

- If hits in the time-of-flight (TOF) detector are associated with the cluster, the measured time at the TOF is required to be less than 2 ns from the expected arrival time of a photon originating from the beam crossing. This cut rejects cosmic ray events and also removes background from antineutrons produced in photon-photon interactions.

- We apply the isolation criterion proposed in [26] to the photon candidate using all detected particles based on the matching algorithm [24]. For each particle $i$, the distance

$$R_{i\gamma} = \sqrt{(\phi_i - \phi_\gamma)^2 + (\eta_i - \eta_\gamma)^2} \tag{2}$$

  to the photon candidate is computed in $\phi\eta$ space, where $\phi$ and $\eta$ are the azimuthal angle and pseudorapidity, respectively. A photon candidate is kept if the condition

$$\sum_{\text{particles},i} E_{\mathrm{T},i}\Theta(\delta - R_{i,\gamma}) \leq 0.2 \cdot E_{\mathrm{T},\gamma}\frac{1-\cos(\delta)}{1-\cos(R)}, \text{ for all } \delta \leq R \tag{3}$$

  is fulfilled, where $E_{\mathrm{T},i}$ is the transverse energy of the $i^{th}$ particle, $\Theta$ is the step function, which ensures that only particles in the cone with opening half-angle $\delta$ contribute to the sum, and the cone radius $R = 1$. Events with more than one isolated photon are rejected.

- The difference between the azimuthal angle $\phi^\gamma$ of the photon candidate and the azimuthal angle of the remaining hadronic system is required to be between $\pi - 1$ and $\pi + 1$.

- Background from events with purely leptonic final states is further reduced by rejecting events where more than 50% of all tracks are identified as electrons using the specific energy loss, $\mathrm{d}E/\mathrm{d}x$, in the jet chamber. For this identification, the $\mathrm{d}E/\mathrm{d}x$ probability for the electron hypothesis should exceed 50%.

After applying all cuts 137 data events are selected.

# 5 Determination of the number of photons

The main background to the prompt photon signal is from photons produced in $\pi^0$ and $\eta$ decays, and from antineutrons, $\bar{\mathrm{n}}$. To separate signal photons from the background, a cluster shape analysis is performed. The cluster shape analysis derives the background rate from the data and is independent of the Monte Carlo predictions for the background rates. Two cluster shape variables are used:

- The sum of the energy-weighted quadratic deviations of the lead-glass block coordinates with respect to the coordinates of the cluster,

$$\sigma_{\mathrm{cluster}} = \frac{\sum_{\mathrm{blocks},i} E_i((\phi_i - \phi_\gamma)^2 + (\theta_i - \theta_\gamma)^2)}{E_\gamma}. \tag{4}$$

- The ratio $f_{\mathrm{max}}$ of the energy of the most energetic block of the cluster to the total cluster energy,

$$f_{\mathrm{max}} = \frac{E_{\mathrm{max}}}{E_\gamma}. \tag{5}$$

To obtain the fraction of prompt photons in the sample of candidates, the normalised two-dimensional distribution of $f_{\mathrm{max}}$ and $\sigma_{\mathrm{cluster}}$ is parametrised as a sum of signal and background contributions:

$$\begin{aligned} g(f_{\mathrm{max}}, \sigma_{\mathrm{cluster}}) = & \\ & a g^{\gamma}(f_{\mathrm{max}}, \sigma_{\mathrm{cluster}}) + b g^{\pi^0}(f_{\mathrm{max}}, \sigma_{\mathrm{cluster}}) + \\ & (1-a-b)(c g^{\eta}(f_{\mathrm{max}}, \sigma_{\mathrm{cluster}}) + (1-c) g^{\bar{\mathrm{n}}}(f_{\mathrm{max}}, \sigma_{\mathrm{cluster}})), \end{aligned} \tag{6}$$

where $g^k(f_{\mathrm{max}}, \sigma_{\mathrm{cluster}})$ denotes the normalised distribution obtained for particle type $k$; $a$ and $b$ denote the $\gamma$ and $\pi^0$ fractions in the candidate sample while $c$ is fixed to match the ratio of events, $N(\eta)/(N(\bar{\mathrm{n}}) + N(\eta))$, predicted by PHOJET for photon-photon events with the same selection criteria as are applied to the data. The one-dimensional distributions of $f_{\mathrm{max}}$ and $\sigma_{\mathrm{cluster}}$ are shown in Fig. 4. The shape of the signal distribution is taken from the detector simulation of the prompt photon signal using PYTHIA. The simulation of the shower-shape variables for single photons has been compared to the shower-shape variables measured for photons in radiative Bhabha events, $\mathrm{e^+e^-} \to \mathrm{e^+e^-}\gamma$, selected from the OPAL data, and is found to be consistent.

A binned maximum likelihood fit is applied to determine the fractions $a$ and $b$, assuming that the content of each bin follows a Poisson distribution. The fit yields a photon contribution of $a = 0.86 \pm 0.08$ (stat) and a $\pi^0$ contribution of $b = 0.12 \pm 0.08$ (stat), where the uncertainties are due to the statistical uncertainties of the data. Within this uncertainty the $\pi^0$ rate is consistent with the $\pi^0$ production cross-section predicted by PHOJET.

# 6 Separation of single and double-resolved events

To study the relative contributions of single and double-resolved processes the variables

$$x_\gamma^\pm = \frac{p_\mathrm{T}^\gamma e^{\pm\eta^\gamma} + p_\mathrm{T}^\mathrm{jet} e^{\pm\eta^\mathrm{jet}}}{y^\pm\sqrt{s_\mathrm{ee}}} \approx \frac{p_\mathrm{T}^\gamma e^{\pm\eta^\gamma} + p_\mathrm{T}^\mathrm{jet} e^{\pm\eta^\mathrm{jet}}}{\Sigma_{\mathrm{hadrons},\gamma}(E \pm p_z)}. \quad (7)$$

can be defined in $\gamma$ plus jet events, where $y^\pm = E_\gamma/E_\mathrm{e}$ are the fractional energies of the quasi-real initial photons oriented towards the positive and negative $z$ axis, and $p_\mathrm{T}$, $\eta$ are the transverse momenta and pseudorapidities of the jet and prompt photon, respectively. Since $y^\pm$ cannot be measured directly, the denominator of Eq. 7 is approximated by summing over the energies $E$ and the $z$ components of the momenta, $p_z$, of all detected final state particles.

The variables $x_\gamma^+$ and $x_\gamma^-$ are measures of the fractions of the initial photons momenta participating in the hard interaction. In LO, $x_\gamma^+$ and $x_\gamma^-$ should be smaller than 1 for double-resolved events, whereas for single-resolved events only one of two variables is smaller than 1 and the other variable, related to the directly interacting photon, equals 1.

In this paper we use similar variables proposed in [9]

$$x_\mathrm{LL}^\pm = \frac{p_\mathrm{T}^\gamma(e^{\pm\eta^\gamma} + e^{\pm\eta^\mathrm{jet}})}{y^\pm\sqrt{s_\mathrm{ee}}} \approx \frac{p_\mathrm{T}^\gamma(e^{\pm\eta^\gamma} + e^{\pm\eta^\mathrm{jet}})}{\Sigma_{\mathrm{hadrons},\gamma}(E \pm p_z)}. \quad (8)$$

where the transverse momentum of the jet has been replaced by the transverse momentum of the prompt photon. Since the transverse momentum is measured with better resolution for a photon than for a jet, the experimental resolution for $x_\mathrm{LL}^\pm$ is better than for $x_\gamma^\pm$.

The jets are reconstructed using a cone algorithm [27]. They are required to have a transverse momentum of $p_\mathrm{T}^\mathrm{jet} > 2.5$ GeV, the pseudorapidity $\eta^\mathrm{jet}$ of the jet must be in the range $[-2, 2]$, and the radius of the cone in $\eta\phi$ space is set to $R = 1$. A lower cut for $p_\mathrm{T}^\mathrm{jet}$ than for $p_\mathrm{T}^\gamma$ is chosen because a symmetric cut $p_\mathrm{T}^\mathrm{jet} = p_\mathrm{T}^\gamma$ leads to infrared instabilities in the NLO calculations.

About 64% of the selected events with a photon have exactly one jet and about 20% have two or more jets. Events with two or more jets are included in the $\gamma$ plus jet sample by evaluating $x_\mathrm{LL}^\pm$ using the jet with the highest transverse momentum.

The fraction of single-resolved events in the $\gamma$ plus jet sample is determined by a binned maximum likelihood fit to the normalised two-dimensional $x_\mathrm{LL}^\pm$ distribution.

$$g(x_\mathrm{LL}^+, x_\mathrm{LL}^-) = rag^\mathrm{sr}(x_\mathrm{LL}^+, x_\mathrm{LL}^-) + (1-r)ag^\mathrm{dr}(x_\mathrm{LL}^+, x_\mathrm{LL}^-) + (1-a)g^\mathrm{bg}(x_\mathrm{LL}^+, x_\mathrm{LL}^-). \quad (9)$$

In the fit the sum of the Monte Carlo distributions for single (sr) and double-resolved (dr) events is fixed to the number of prompt photons in the data, obtained by the shower-shape analysis. The fraction $1 - a$ of $\pi^0$, $\eta$, and $\bar{\mathrm{n}}$ background (bg) events is also fixed to the value derived from the shower-shape fit. The shape of the $x_\mathrm{LL}^\pm$ distributions for the single and double-resolved events is taken from PYTHIA and for the background events from PHOJET. The only free parameter is the fraction $r$ of single-resolved events in the selected data sample. The fit yields a fraction of single-resolved events $r = 0.47 \pm 0.11$ (stat).

In the original PYTHIA simulation the rate of single-resolved events is predicted to be one order of magnitude larger than the rate of double-resolved events. A good description of the data by the Monte Carlo simulation is necessary to determine the correction factors for acceptance losses and resolution effects. The rate of single-resolved events in PYTHIA after the detector simulation and event selection is therefore adjusted to the fitted value $r = 0.47 \pm 0.11$ (stat). Fig. 5 shows the $x_{\rm LL}^{\rm max} = \max(x_{\rm LL}^{+}, x_{\rm LL}^{-})$ and $x_{\rm LL}^{\rm min} = \min(x_{\rm LL}^{+}, x_{\rm LL}^{-})$ distributions compared to the PYTHIA simulation using $r = 0.47 \pm 0.11$ (stat). The sum of the signal and background Monte Carlo distributions is normalized to the data. The fraction of the $\pi^0$, $\eta$ and $\bar{\rm n}$ background is taken from the shower-shape fit.

The $x_{\rm LL}^{\rm max}$ distribution is described well by the sum of signal and background Monte Carlo after the fit, whereas the $x_{\rm LL}^{\rm min}$ distribution has a slight enhancement of low values of $x_{\rm LL}^{\rm min}$, in the region where both single and double-resolved events contribute.

A variable similar to $x_{\rm LL}^{\pm}$ which is defined for all prompt photon events, not just the subsample with jets, is the scaled transverse momentum $x_{\rm T}^{\gamma}$ of the prompt photon. It is given by

$$x_{\rm T}^{\gamma} = \frac{2p_{\rm T}^{\gamma}}{W}. \tag{10}$$

For events with a photon and a centrally produced jet ($\eta^{\gamma} = \eta^{\rm jet} = 0$), the variable $x_{\rm T}^{\gamma}$ is equal to $x_{\gamma}^{\pm}$. This variable is therefore also sensitive to the fractions of the single-resolved and the double-resolved processes. As with the $x_{\gamma}^{\pm}$ distribution, the single-resolved contribution dominates at higher values of $x_{\rm T}^{\gamma}$, whereas the double-resolved events are concentrated at smaller $x_{\rm T}^{\gamma}$, as predicted by the Monte Carlo.

# 7 Systematic uncertainties

Several kinematic distributions are shown in Fig. 6 to demonstrate the general agreement between the Monte Carlo and data distributions. The distributions of the charged multiplicity, $n_{\rm ch}$, the visible invariant mass, $W_{\rm vis}$, the thrust in the $r\phi$ plane, $T_{r\phi}$, and the angle between the prompt photon and the remaining hadronic system in the $r\phi$ plane are shown after the event selection. The sum of the signal and background Monte Carlo is normalised to the data. The transverse energy flow around the isolation cone, $1/N_{\gamma} \cdot {\rm d}E_{T,i}/{\rm d}R_{i\gamma}$, is shown in Fig. 7. The fraction of single-resolved events is taken from the fit to the $x_{\rm LL}^{\pm}$ distribution and the fraction of $\pi^0$, $\eta$ and $\bar{\rm n}$ background is taken from the shower-shape fit (Eq. 6). The shape of the $\pi^0$, $\eta$ and $\bar{\rm n}$ background distributions is simulated using PHOJET. The Monte Carlo simulation describes the data well for all the distributions shown.

The following systematic uncertainties are studied in detail:

- The background from $\pi^0$ decays with a single photon in the isolation cone is irreducible. It is determined to be $N_{\pi^0 \to 1\gamma}^{\rm data} = 14 \pm 10$ (stat) using the fit to the shower-shape variables. The uncertainty on this background is estimated using the following procedure:
  - A $\pi^0$ peak is reconstructed using data events with two photons in the cone. Taking the ratio of $\pi^0$ events with one and two photons in the cone from the PHOJET

simulation, the $\pi^0$ background is estimated to be

$$N^{\mathrm{data}}_{\pi^0\to 1\gamma} = N^{\mathrm{data}}_{\pi^0\to 2\gamma}\frac{N^{\mathrm{PHOJET}}_{\pi^0\to 1\gamma}}{N^{\mathrm{PHOJET}}_{\pi^0\to 2\gamma}} = 18 \pm 3 \text{ (stat)}. \tag{11}$$

– Due to isospin conservation the cross-sections and fragmentation functions for $\pi^0$ and $\pi^\pm$ production are expected to be proportional to each other. The analysis is therefore redone with the same selection cuts except that an isolated track has to be found instead of a photon. The track is identified as a charged pion using the specific energy loss $\mathrm{d}E/\mathrm{d}x$ measured in the jet chamber. With these cuts the measured ratio of the number of charged to neutral pions is found to be $11 \pm 3$ (stat) for the PHOJET simulation and $12 \pm 9$ (stat) for the data.

An uncertainty of 50% is assigned to the $\pi^0$ background rate which is mainly due to the large statistical uncertainty of the tests performed. The resulting uncertainty on the total cross-section is 8.3%.

- The influence of the calibration of the ECAL on the selection efficiencies is determined by varying the energy of the lead-glass blocks by ±3% for the data [28]. The efficiencies obtained are compared to the original values and the difference is assigned as systematic uncertainty of 7.0%.

- The fraction of single-resolved events is determined with the variable $x^{\pm}_{\mathrm{LL}}$ to be $r = 0.47 \pm 0.11$ (stat). The systematic uncertainty is determined by fitting the $x_\gamma$ and $x^\gamma_{\mathrm{T}}$ distributions defined in Section 6. These fits yield $r = 0.64 \pm 0.12$ (stat) and $r = 0.43 \pm 0.08$ (stat), respectively. The value of $r$ is varied in the range $0.30 < r < 0.67$ within the full uncertainty given by the largest deviation of the two fit results from the value $r = 0.47$ used in the analysis. Since the efficiencies are not very different for single and double-resolved events, this leads to an uncertainty of only 4.0% for the total cross-section.

- The influence of the modeling of the parton density functions is studied by using Monte Carlo samples generated with the GRV-LO and LAC-1 parametrisations of the parton density functions. This yields a systematic uncertainty of 3.8%.

- Using HERWIG instead of PYTHIA for the simulation of single-resolved events changes the measured prompt photon production cross-section by 3.8%.

- To estimate the effect of the fixed $\eta$ to $\bar{\mathrm{n}}$ ratio, fits to the distributions of the shower-shape variables are applied with either no $\bar{\mathrm{n}}$ or no $\eta$ background. This affects the signal-to-background ratio by 2.0%.

- The sensitivity of the shower-shape variables to the exponential weighting functions for the distributions of the single particle generator events is estimated as follows. The parameters of the exponential functions are determined by a fit of the single particle generator $p_{\mathrm{T}}$ distribution to the PHOJET $p_{\mathrm{T}}$ distributions for the same particle type. The parameters of the weighting function are scaled to $(1 \pm \alpha)$, where $\alpha$ is the relative error of the fitted weighting parameter. The shower-shape distributions are re-weighted with the functions using the scaled parameter, and the analysis is redone. The resulting systematic uncertainty is 2.8%.

- The dependence of the shower-shape variables on the number of required lead-glass blocks is studied by increasing the cut on the number of lead-glass blocks from 2 to 3 in the Monte Carlo but not in the data. This changes the signal-to-background ratio by 1.8%.
- The finite number of Monte Carlo events yields a systematic error of 1.6%.
- The fits to the distributions of the shower-shape variables are performed with various bin sizes and upper and lower bounds of the histograms. The bins sizes were doubled/halved and the histogram bounds were shifted by half a bin size. This changes the signal contribution parameter $a$ by 1.3%.
- The analysis is repeated using only the cluster shape variable $C$ [29]. The variable $C$ is the result of a Monte Carlo fit which compares the measured to the expected energies. The $\pi^0 : \eta : \bar{\text{n}}$ ratio is fixed to the values obtained in the shower-shape analysis above. The measured signal contribution changes by 0.5%.
- The resolution of the angular distance in the $r\phi$ plane between the photon and the hadronic system is approximately 5%. The systematic uncertainty is obtained by changing the cut on this variable by $\pm 5\%$ for the Monte Carlo events while leaving it unchanged in the data. This changes the cross-section by 0.2%.
- The contribution from photon-photon events with a photon from initial state radiation in the signal region was determined to be negligible using the BDK Monte Carlo [17]. The contribution of events with final state radiation (FSR) to the data sample is estimated to be about $10 - 15\%$ using PHOJET. The kinematic properties of these events are very similar to the single-resolved signal events. Performing the measurement with and without taking into account the FSR contribution leads to a negligible change in the measured cross-section.

The resulting systematic uncertainties are summarised in Table 1.

# 8 Total cross-section

The total inclusive cross-section for isolated prompt photon production with $p_{\text{T}}^{\gamma} > 3$ GeV and $|\eta^{\gamma}| < 1$ is obtained using

$$\sigma_{\text{tot}} = \left( \frac{r}{\epsilon_{\text{single}}} + \frac{1-r}{\epsilon_{\text{double}}} \right) \frac{N_{\text{prompt}}}{\mathcal{L}}. \tag{12}$$

The number of remaining prompt photons after the subtraction of $\pi^0$, $\eta$, and $\bar{\text{n}}$ background is denoted by $N_{\text{prompt}}$, and the single-resolved contribution $r$ is taken from the result of the fit to the two-dimensional $x_{\text{LL}}^{\pm}$ distribution. The efficiencies $\epsilon_{\text{single}}$ and $\epsilon_{\text{double}}$ are defined as the total number of selected events divided by the total number of generated events with an isolated prompt photon in the range $p_{\text{T}}^{\gamma} > 3.0$ GeV and $|\eta^{\gamma}| < 1$ for the single and double-resolved PYTHIA Monte Carlo samples. The efficiencies are determined to be $\epsilon_{\text{single}} = (51.8 \pm 0.7\ (\text{stat}))\%$ and $\epsilon_{\text{double}} = (61.8 \pm 1.1\ (\text{stat}))\%$. This yields the cross-section

$$\sigma_{\text{tot}} = 0.32 \pm 0.04\ (\text{stat}) \pm 0.04\ (\text{sys})\ \text{pb} \tag{13}$$

in the kinematic range defined by the anti-tagging condition.

# 9 Differential cross-section

To correct the measured differential cross-sections for acceptance losses and resolution effects in the detector, correction factors are determined in each bin using the Monte Carlo simulation. The variables are first corrected event by event for the average offset of the measured value in each bin with respect to the generated value. The resulting distribution is then multiplied by a bin-by-bin efficiency. The dependence of the corrected distributions on the shape of the generated Monte Carlo distributions is studied by reweighting the generated distributions. The changes are found to be small compared to the total uncertainties.

The inclusive differential cross-sections $\mathrm{d}\sigma/\mathrm{d}p_{\mathrm{T}}^{\gamma}$ and $\mathrm{d}\sigma/\mathrm{d}|\eta^{\gamma}|$ for isolated prompt photon production are given in Table 2. The bin size is chosen to be significantly larger than the experimental resolution, which is about 200-300 MeV for $p_{\mathrm{T}}^{\gamma}$. The $\eta^{\gamma}$ resolution is much smaller than the bin size due to the high ECAL granularity.

The fractions of single and double-resolved Monte Carlo events are determined using the measured $x_{\mathrm{LL}}^{\pm}$ distribution (Section 6). The systematic uncertainties related to the determination of this ratio, to the ECAL calibration, and to the modeling of the parton densities have been determined for each bin separately, whereas all other systematic uncertainties are added globally.

In Figs. 8 and 9, the inclusive differential cross-sections $\mathrm{d}\sigma/\mathrm{d}p_{\mathrm{T}}^{\gamma}$ and $\mathrm{d}\sigma/\mathrm{d}|\eta^{\gamma}|$ are compared to the prediction of the Monte Carlo generator PYTHIA and to the NLO calculation. For the PYTHIA simulation the SAS-1D parametrisation [12] is used with the original ratio of the single to double-resolved contribution given by PYTHIA. The NLO calculation uses the AFG02 [30] parametrisation of the parton distributions of the photon with $\Lambda_{\overline{\mathrm{MS}}}^{(4)} = 300$ MeV and $Q_{\mathrm{max}}^2 = 10$ GeV$^2$. The factorisation and renormalisation scales are set equal to $p_{\mathrm{T}}^{\gamma}$. The calculated cross-sections are integrals over the bins used in the analysis.

In both cases PYTHIA reproduces the shape of the distributions well but underestimates the cross-sections, whereas the NLO calculation [9] describes well the shape and normalisation of the data. The differential cross-section $\mathrm{d}\sigma/\mathrm{d}|\eta^{\gamma}|$ is independent of $|\eta^{\gamma}|$ within the experimental uncertainties. This effect is mainly due to the event-by-event variation of the Lorentz boost from the $\gamma\gamma$ system to the laboratory system. The NLO and LO calculations using the AFG02 [30] and GRV-HO [13] parametrisations are also shown in Fig. 9. For this LO calculation the Born terms are used for the subprocess cross sections together with the NLO strong coupling constant, $\alpha_{\mathrm{s}}$, and the NLO parton distribution functions.

The difference between the cross-sections using the two parametrisations is small in comparison to the uncertainty of the data.

The differential cross-section $\mathrm{d}\sigma/\mathrm{d}x_{\mathrm{T}}^{\gamma}$ is shown in Fig. 10 and the values are given in Table 2. The experimental resolution is in the range 0.05 to 0.15. At low values of $x_{\mathrm{T}}^{\gamma}$ the data lie about two standard deviations above the NLO calculation which indicates a higher double-resolved contribution. The lowest kinematically accessible value is approximately $x_{\mathrm{T}}^{\gamma} = 2p_{\mathrm{T}}^{\gamma}/W \simeq 0.1$.

The differential cross-section $\mathrm{d}\sigma/\mathrm{d}x_{\mathrm{LL}}^{-}$ for the production of a prompt photon in association with at least one jet in the kinematic range $|\eta^{\gamma}| < 1$, $p_{\mathrm{T}}^{\gamma} > 3.0$ GeV, $|\eta^{\mathrm{jet}}| < 2$, and $p_{\mathrm{T}}^{\mathrm{jet}} > 2.5$ GeV

is shown in Fig. 11. The values are given in Table 3. If there are two jets associated with the photon, the photon plus jets cross-section is defined by keeping the jet with the highest $p_{\mathrm{T}}^{\mathrm{jet}}$. The same procedure is used in the NLO calculation.

For the measurement of $\mathrm{d}\sigma/\mathrm{d}x_{\mathrm{LL}}^{-}$ an additional normalisation uncertainty of 10% due to the jet requirement needs to be taken into account [1]. The main additional sources of this uncertainty are the energy scale of the calorimeter, which is known to about 3%, and the model dependence of the jet fragmentation [1].

All measured cross-sections are given at the hadron level, i.e., no hadronisation corrections are applied to the data. The hadron level cross-sections are compared to the parton level calculations by Fontannaz et al. [9] in Fig. 11. A comparison of the PYTHIA parton and hadron cross-sections in Fig. 11 shows the size of hadronisation corrections for this particular Monte Carlo model.

In the region $x_{\mathrm{LL}}^{\pm} > 0.625$, the peak around $x_{\mathrm{LL}}^{\pm} = 1$ in the LO calculations is smeared out towards lower values of $x_{\mathrm{LL}}^{\pm}$ both by the hadronisation effects in the PYTHIA simulation and by the higher order effects included in the NLO calculation. In this region PYTHIA and the NLO calculation give a good description of the data within the large uncertainties. For $x_{\mathrm{LL}}^{\pm} < 0.625$ hadronisation effects are expected to be smaller. The NLO cross-section is larger than the LO cross-sections in this kinematic range, in better agreement with the data.

# 10 Conclusion

The inclusive cross-section for the production of isolated prompt photons in anti-tagged $\gamma\gamma$ collisions is measured using the OPAL detector at LEP. Data with an integrated luminosity of 648.6 pb$^{-1}$ with centre-of-mass energies $\sqrt{s_{\mathrm{ee}}}$ from 183 GeV to 209 GeV are used.

The prompt photons are selected by requiring the isolation criterion of [26]. The signal and the background from $\pi^0, \eta$ and $\bar{\mathrm{n}}$ production are separated by a cluster shape analysis. In the kinematic region $p_{\mathrm{T}}^{\gamma} > 3.0$ GeV and $|\eta^{\gamma}| < 1$, a total of 110.8 events remain after background subtraction. The total cross-section for inclusive isolated prompt photon production in the kinematic range defined by these cuts and by the anti-tagging condition is measured to be

$$\sigma_{\mathrm{tot}} = 0.32 \pm 0.04\ (\mathrm{stat}) \pm 0.04\ (\mathrm{sys})\ \mathrm{pb}. \tag{14}$$

The anti-tagging cuts corresponds to $Q^2_{\mathrm{max}} \approx 10\ \mathrm{GeV}^2$.

Single and double-resolved events are separated using photon plus jet events, where the jets have been reconstructed with a cone jet algorithm. For the first time the differential cross-sections as a function of the transverse momentum, $\mathrm{d}\sigma/\mathrm{d}p_{\mathrm{T}}^{\gamma}$, the pseudorapidity, $\mathrm{d}\sigma/\mathrm{d}|\eta^{\gamma}|$, and the scaled transverse momentum, $\mathrm{d}\sigma/\mathrm{d}x_{\mathrm{T}}^{\gamma}$, are measured and compared to the predictions of PYTHIA and to a NLO calculation. In addition, we measure the differential cross-section $\mathrm{d}\sigma/\mathrm{d}x_{\mathrm{LL}}^{-}$ for the production of a prompt photon in association with at least one jet in the kinematic range $|\eta^{\mathrm{jet}}| < 2$ and $p_{\mathrm{T}}^{\mathrm{jet}} > 2.5$ GeV. The NLO calculation gives a better description of the data than the LO calculation and the PYTHIA Monte Carlo, especially at low $x_{\mathrm{LL}}^{\pm}$.

# Acknowledgements

We thank Michel Fontannaz and Gudrun Heinrich for very helpful discussions and for providing the NLO calculations.

We particularly wish to thank the SL Division for the efficient operation of the LEP accelerator at all energies and for their close cooperation with our experimental group. In addition to the support staff at our own institutions we are pleased to acknowledge the
Department of Energy, USA,
National Science Foundation, USA,
Particle Physics and Astronomy Research Council, UK,
Natural Sciences and Engineering Research Council, Canada,
Israel Science Foundation, administered by the Israel Academy of Science and Humanities,
Benoziyo Center for High Energy Physics,
Japanese Ministry of Education, Culture, Sports, Science and Technology (MEXT) and a grant under the MEXT International Science Research Program,
Japanese Society for the Promotion of Science (JSPS),
German Israeli Bi-national Science Foundation (GIF),
Bundesministerium für Bildung und Forschung, Germany,
National Research Council of Canada,
Hungarian Foundation for Scientific Research, OTKA T-038240, and T-042864,
The NWO/NATO Fund for Scientific Reasearch, the Netherlands.

# References


[1] OPAL Collab., G. Abbiendi et al., *Di-Jet Production in Photon-Photon Collisions at* $\sqrt{s}_{ee}$ *from 189 to 209 GeV*, submitted to Eur. Phys. J. C;
OPAL Collab., G. Abbiendi et al., Eur. Phys. J. C10 (1999) 547;
OPAL Collab., K. Ackerstaff et al., Z. Phys. C73 (1997) 433.

[2] OPAL Collab., G. Abbiendi et al., Eur. Phys. J. C6 (1999) 253.

[3] OPAL Collab., G. Abbiendi et al., Eur. Phys. J. C16 (2000) 579.

[4] M. Drees and R.M. Godbole, Phys. Lett. B257 (1991) 425.

[5] L.E. Gordon and J.K. Storrow, Phys. Lett. B385 (1996) 385.

[6] NA14 Collab., E. Auge et al., Phys. Lett. B182 (1986) 409;
NA14 Collab., P. Astbury et al., Phys. Lett. B152 (1985) 419.

[7] ZEUS Collab., S. Chekanov et al., Phys. Lett. B511 (2001) 19;
ZEUS Collab., J. Breitweg et al., Phys. Lett. B472 (2000) 175;
ZEUS Collab., J. Breitweg et al., Phys. Lett. B413 (1997) 201.

[8] T. Sjöstrand, Comp. Phys. Comm. 82 (1994) 74.

[9] M. Fontannaz, J.P. Guillet and G. Heinrich, Eur. Phys. J. C23 (2002) 503, and private communications.

[10] OPAL Collab., K. Ahmet et al., Nucl. Instr. and Methods A305 (1991) 275;
P.P. Allport et al., Nucl. Instr. and Methods A346 (1994) 476;
P.P. Allport et al., Nucl. Instr. and Methods A324 (1993) 34;
O. Biebel et al., Nucl. Instr. and Methods A323 (1992) 169;
M. Hauschild et al., Nucl. Instr. and Methods A314 (1992) 74.

[11] B.E. Anderson et al., IEEE Trans. Nucl. Sci. 41 (1994) 845.

[12] G.A. Schuler and T. Sjöstrand, Z. Phys. C68 (1995) 607.

[13] M. Glück, E. Reya and A. Vogt, Phys. Rev. D46 (1992) 1973;
M. Glück, E. Reya and A. Vogt, Phys. Rev. D45 (1992) 3986.

[14] H. Abramowicz, K. Charchula and A. Levy, Phys. Lett. B269 (1991) 458.

[15] G. Marchesini et al., Comp. Phys. Comm. 67 (1992) 465.

[16] R. Engel, Z. Phys. C66 (1995) 203;
R. Engel and J. Ranft, Phys. Rev. D54 (1996) 4244.

[17] F.A. Berends, P.H. Daverveldt and R. Kleiss, Nucl. Phys. B253 (1985) 421;
F.A. Berends, P.H. Daverveldt and R. Kleiss, Comp. Phys. Comm. 40 (1986) 271, 285 and 309.

[18] J. Smith, J.A.M. Vermaseren and G. Grammer Jr., Phys. Rev. D15 (1977) 3280;
J.A.M. Vermaseren, J. Smith and G. Grammer Jr., Phys. Rev. D19 (1979) 137;
J.A.M. Vermaseren, Nucl. Phys. B229 (1983) 347;
R. Bhattacharya, G. Grammer Jr. and J. Smith, Phys. Rev. D15 (1977) 3267.

[19] S. Jadach, B.F.L. Ward and Z. Wąs, Comp. Phys. Comm. 130 (2000) 260.

[20] S. Jadach, B.F.L. Ward and Z. Wąs, Comp. Phys. Comm. 79 (1994) 503.

[21] J. Fujimoto et al., Comp. Phys. Comm. 100 (1997) 128.

[22] S. Jadach, W. Placzek, M. Skrzypek, B.F.L. Ward and Z. Wąs, Comp. Phys. Comm. 119 (1999) 272.

[23] J. Allison et al., Nucl. Instr. and Methods. A317 (1992) 47.

[24] OPAL Collab., G. Alexander et al., Phys. Lett. B377 (1996) 181.

[25] OPAL Collab., G. Abbiendi et al., Eur. Phys. J. C5 (1998) 411.

[26] S. Frixione, Phys. Lett. B429 (1998) 369.

[27] OPAL Collab., R. Akers et al., Z. Phys. C63 (1994) 197.

[28] OPAL Collab., G. Abbiendi et al., Eur. Phys. J. C14 (2000) 199.

[29] OPAL Collab., K. Ackerstaff et al., Eur. Phys. J. C2 (1998) 39.

[30] P. Aurenche, J.P. Guillet and M. Fontannaz, Z. Phys. C64 (1994) 621;
P. Aurenche, J.P. Guillet and M. Fontannaz, in preparation.

| source | uncertainty |
|---|---|
| $\pi^0$ background | 8.3% |
| ECAL calibration | 7.0% |
| ratio single to double-resolved contribution | 4.0% |
| parton density functions | 3.8% |
| HERWIG instead of PYTHIA | 3.8% |
| fixed $\eta : \bar{\text{n}}$ ratio | 2.0% |
| re-weighting of single particle MC | 2.8% |
| minimum number of lead-glass blocks | 1.8% |
| Monte Carlo statistics | 1.6% |
| binning effects | 1.3% |
| using $C$ parameter | 0.5% |
| resolution of $\phi^{\text{hadrons}} - \phi^{\gamma}$ | 0.2% |
| total systematic uncertainty | 13.5% |

Table 1: Relative systematic uncertainties on the total prompt photon cross-section, $\sigma_{\text{tot}}$.

| $p_{\mathrm{T}}^{\gamma}$ [GeV] | $\mathrm{d}\sigma/\mathrm{d}p_{\mathrm{T}}^{\gamma}$ [pb/GeV] |
|---|---|
| 3.0 – 4.0 | $0.153 \pm 0.022 \pm 0.023$ |
| 4.0 – 5.0 | $0.036 \pm 0.010 \pm 0.005$ |
| 5.0 – 6.0 | $0.045 \pm 0.012 \pm 0.006$ |
| 6.0 – 8.0 | $0.016 \pm 0.011 \pm 0.003$ |
| 8.0 – 13.0 | $0.006 \pm 0.010 \pm 0.001$ |
| $\lvert\eta^{\gamma}\rvert$ | $\mathrm{d}\sigma/\mathrm{d}\lvert\eta^{\gamma}\rvert$ [pb] |
| 0.0 – 0.2 | $0.25 \pm 0.06 \pm 0.03$ |
| 0.2 – 0.4 | $0.33 \pm 0.07 \pm 0.06$ |
| 0.4 – 0.6 | $0.18 \pm 0.05 \pm 0.03$ |
| 0.6 – 0.8 | $0.44 \pm 0.09 \pm 0.06$ |
| 0.8 – 1.0 | $0.35 \pm 0.10 \pm 0.05$ |
| $x_{\mathrm{T}}^{\gamma}$ | $\mathrm{d}\sigma/\mathrm{d}x_{\mathrm{T}}^{\gamma}$ [pb] |
| 0.00 – 0.26 | $0.53 \pm 0.09 \pm 0.07$ |
| 0.26 – 0.52 | $0.41 \pm 0.07 \pm 0.05$ |
| 0.52 – 0.78 | $0.30 \pm 0.06 \pm 0.05$ |
| 0.78 – 1.04 | $0.06 \pm 0.05 \pm 0.01$ |

Table 2: Differential cross-sections $\mathrm{d}\sigma/\mathrm{d}p_{\mathrm{T}}^{\gamma}$, $\mathrm{d}\sigma/\mathrm{d}\lvert\eta^{\gamma}\rvert$ and $\mathrm{d}\sigma/\mathrm{d}x_{\mathrm{T}}^{\gamma}$ for $\lvert\eta^{\gamma}\rvert < 1$ and $p_{\mathrm{T}}^{\gamma} > 3$ GeV with the statistical and systematic uncertainties.

| $x_{\mathrm{LL}}^{-}$ | $\mathrm{d}\sigma/\mathrm{d}x_{\mathrm{LL}}^{-}$ [pb] |
|---|---|
| 0.0000 – 0.3125 | $0.24 \pm 0.05 \pm 0.04$ |
| 0.3125 – 0.6250 | $0.20 \pm 0.05 \pm 0.03$ |
| 0.6250 – 0.8750 | $0.26 \pm 0.05 \pm 0.04$ |
| 0.8750 – 1.1250 | $0.25 \pm 0.08 \pm 0.08$ |

Table 3: Differential cross-section $\mathrm{d}\sigma/\mathrm{d}x_{\mathrm{LL}}^{-}$ for $\lvert\eta^{\gamma}\rvert < 1$, $p_{\mathrm{T}}^{\gamma} > 3.0$ GeV, $\lvert\eta^{\mathrm{jet}}\rvert < 2$, and $p_{\mathrm{T}}^{\mathrm{jet}} > 2.5$ GeV. The statistical and systematic uncertainties are also given.

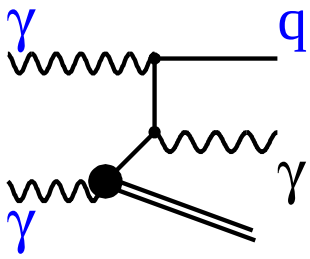


Figure 1: Diagram of the single-resolved process. The double line indicates the photon remnant and the dark circle a resolved photon.

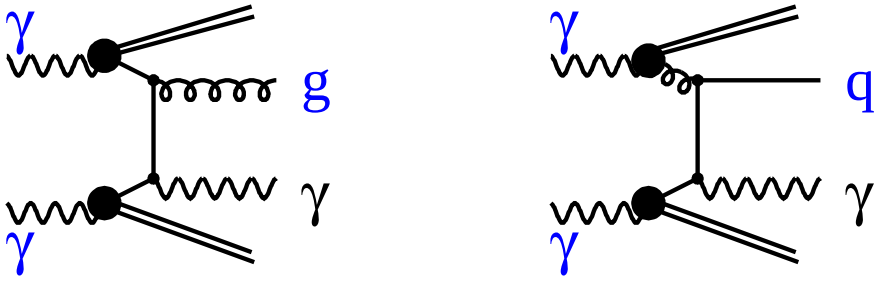


Figure 2: Diagrams of double-resolved processes. The double lines indicate the photon remnant and the dark circles a resolved photon.

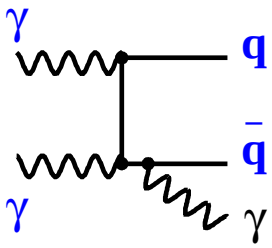


Figure 3: Diagram of a direct process with Final State Radiation (FSR).

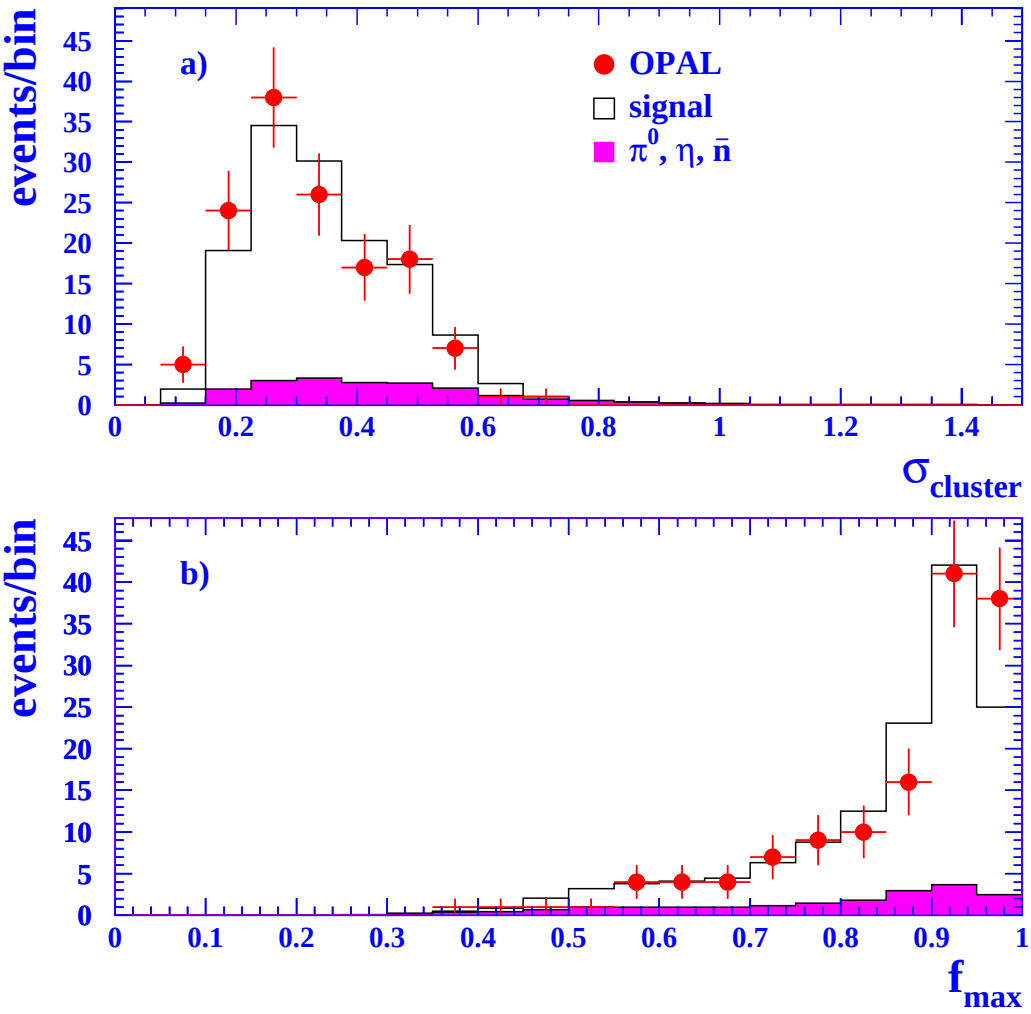


Figure 4: Distributions of the shower-shape variables for data and Monte Carlo events: a) sum of the energy-weighted quadratic deviations of the lead-glass block coordinates with respect to the coordinates of the cluster, $\sigma_{\rm cluster}$; b) ratio of the energy of the most energetic block of the cluster to the total cluster energy, $f_{\rm max}$. The ratio of signal to background is determined by a binned maximum likelihood fit to the two-dimensional distribution.

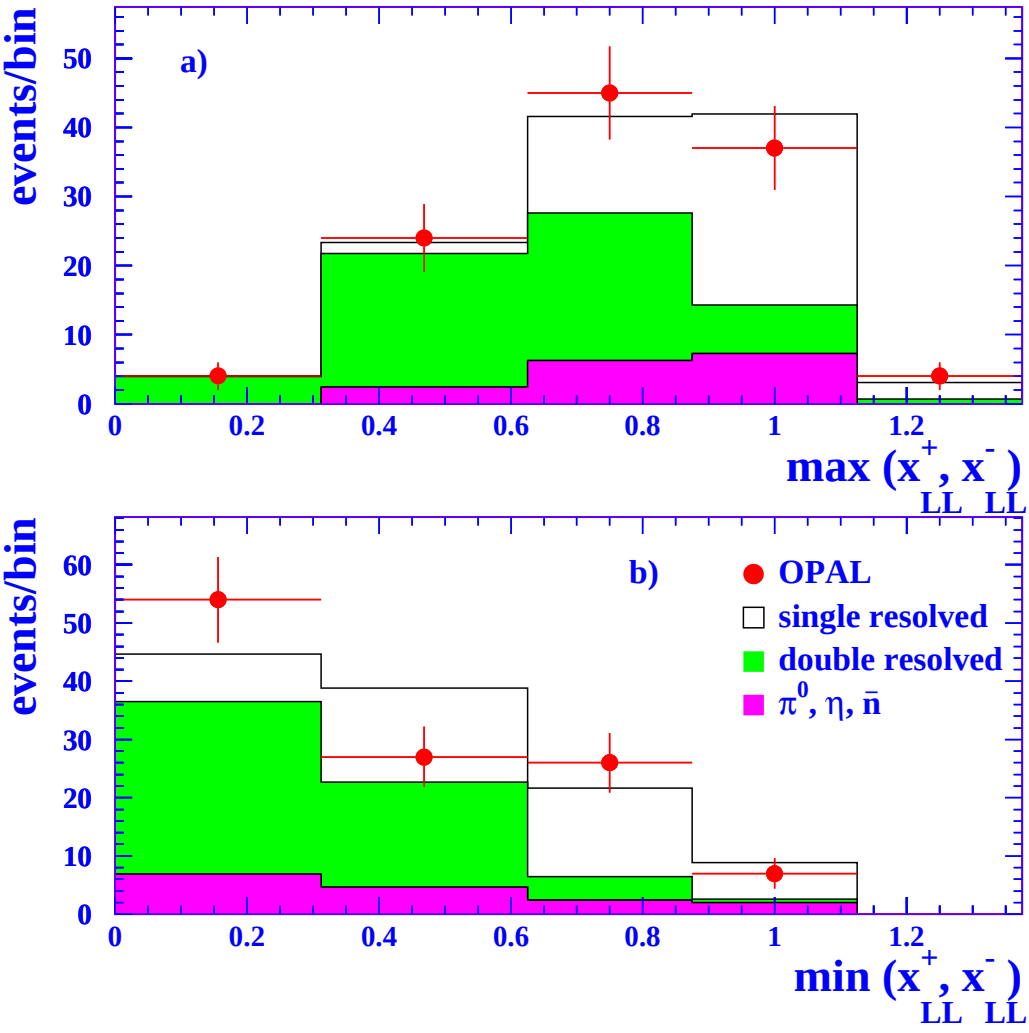


Figure 5: Distribution of the a) maximum and b) minimum of $x^+_{\rm LL}$ and $x^-_{\rm LL}$ for the selected $\gamma$ plus jet events. The uncorrected data distributions are compared to the sum of the single and double-resolved signal Monte Carlo distributions, and the background Monte Carlo distributions. The sum of the signal and background Monte Carlo distributions is normalized to the data. The background fraction is taken from the shower-shape fit and the fraction of single-resolved signal events is taken from the fit to the $x^\pm_{\rm LL}$ distribution.

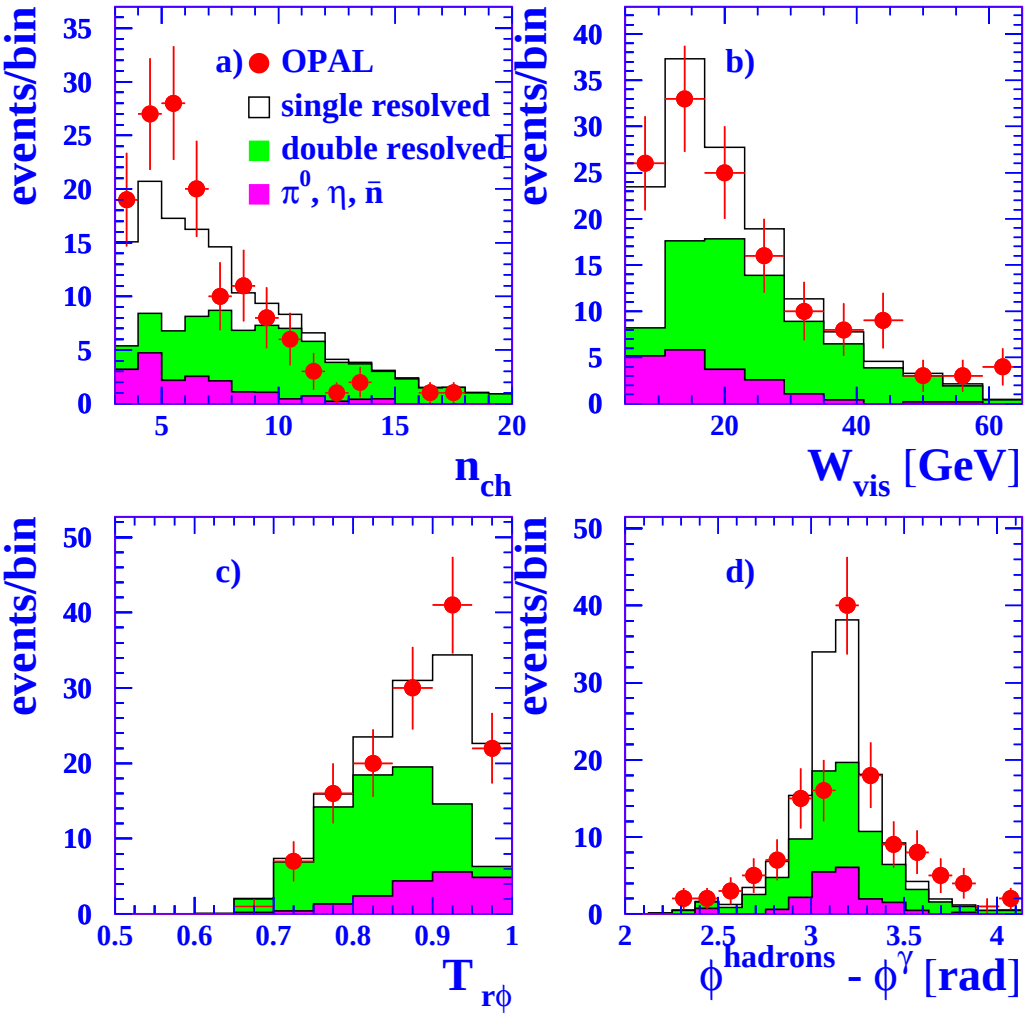


Figure 6: Distributions of a) the charged multiplicity, $n_{\rm ch}$, b) the visible invariant mass, $W_{\rm vis}$, c) the thrust in the $r\phi$ plane, $T_{r\phi}$, and d) the angle between the prompt photon and the remaining hadronic system in the $r\phi$ plane. The sum of the signal and background Monte Carlo distributions is normalized to the data. The background fraction is taken from the shower-shape fit and the fraction of single-resolved signal events is taken from the fit to the $x_{\rm LL}^{\pm}$ distribution.

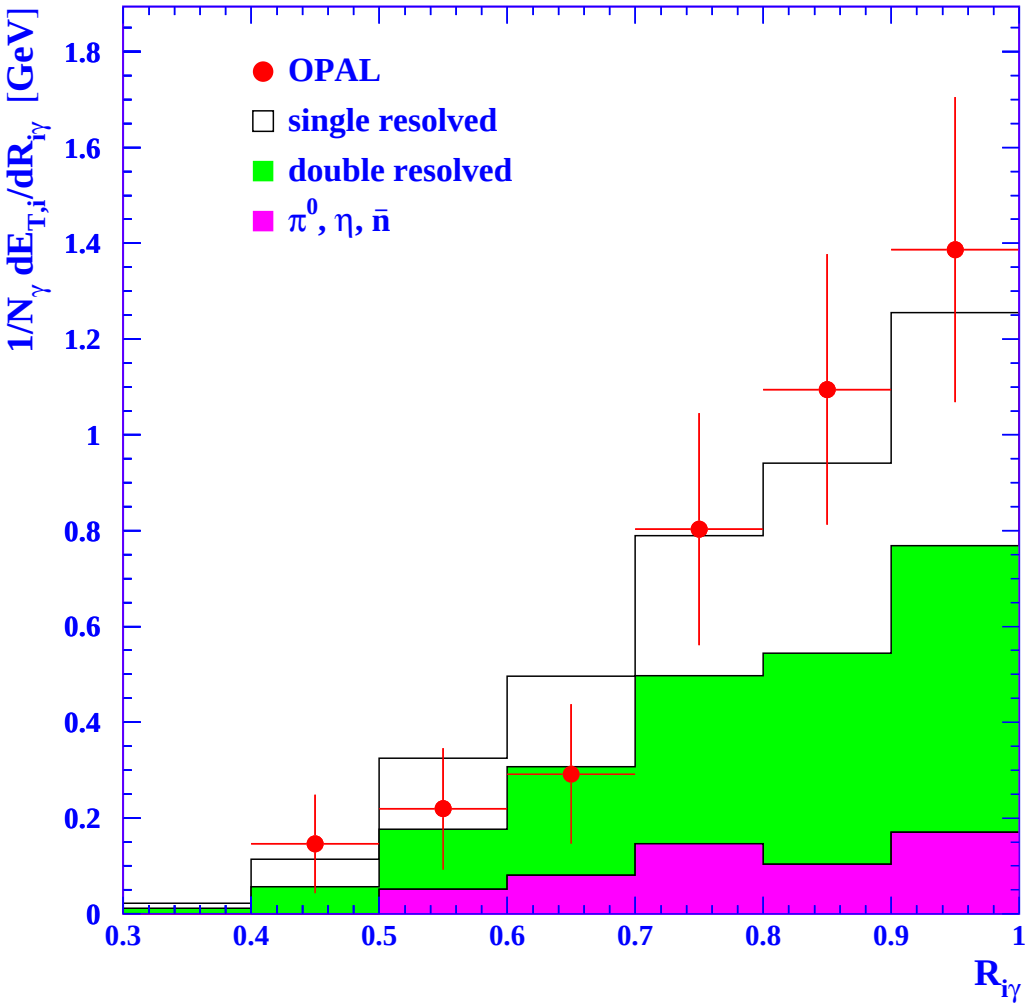


Figure 7: Transverse energy flow around the isolation cone for the selected events. The background fraction is taken from the shower-shape fit and the fraction of single-resolved signal events is taken from the fit to the $x_{\mathrm{LL}}^{\pm}$ distribution.

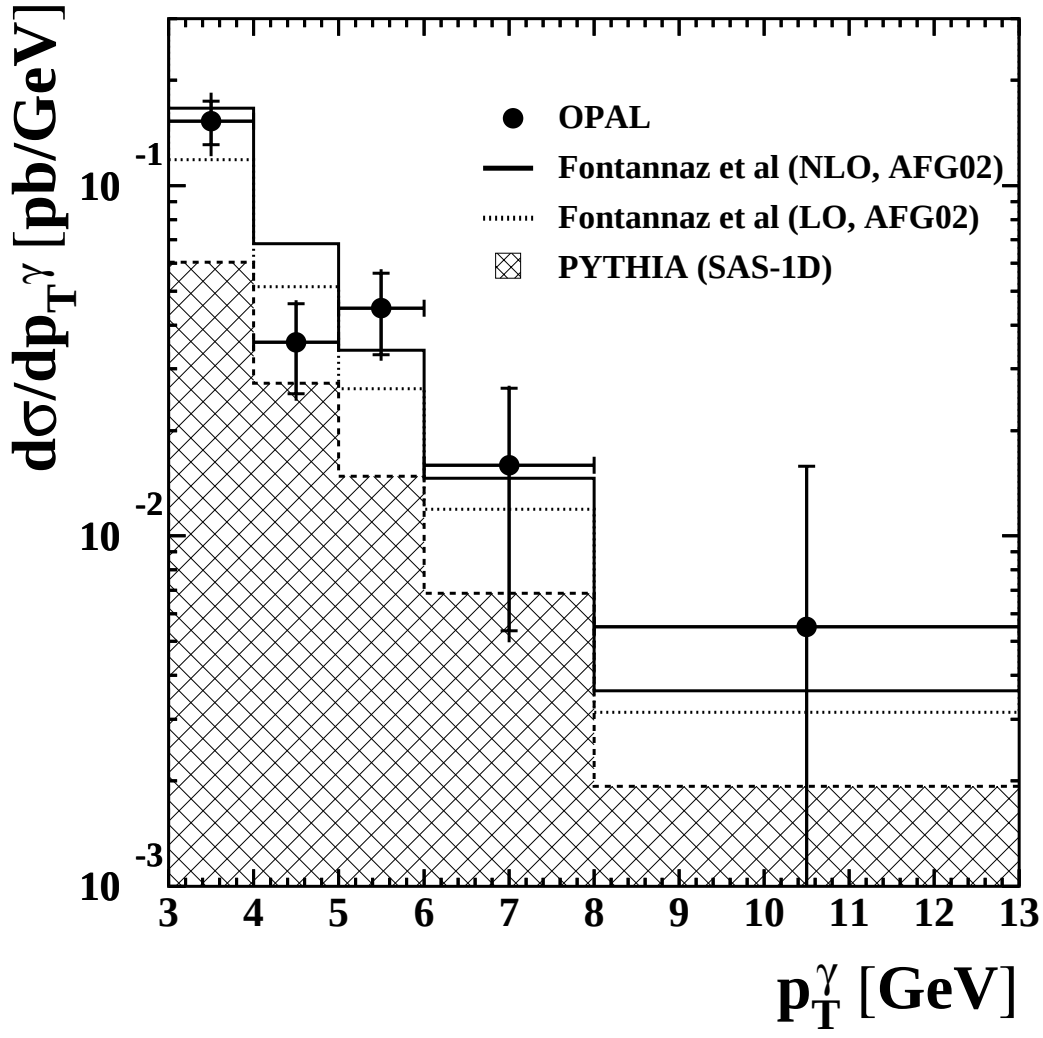


Figure 8: Differential cross-section $\mathrm{d}\sigma/\mathrm{d}p_{\mathrm{T}}^{\gamma}$ for inclusive prompt photon production in the kinematic range $|\eta^{\gamma}| < 1$ and $p_{\mathrm{T}}^{\gamma} > 3.0$ GeV. The points represent data. The inner error bars show the statistical uncertainty and the outer error bars the total uncertainty.

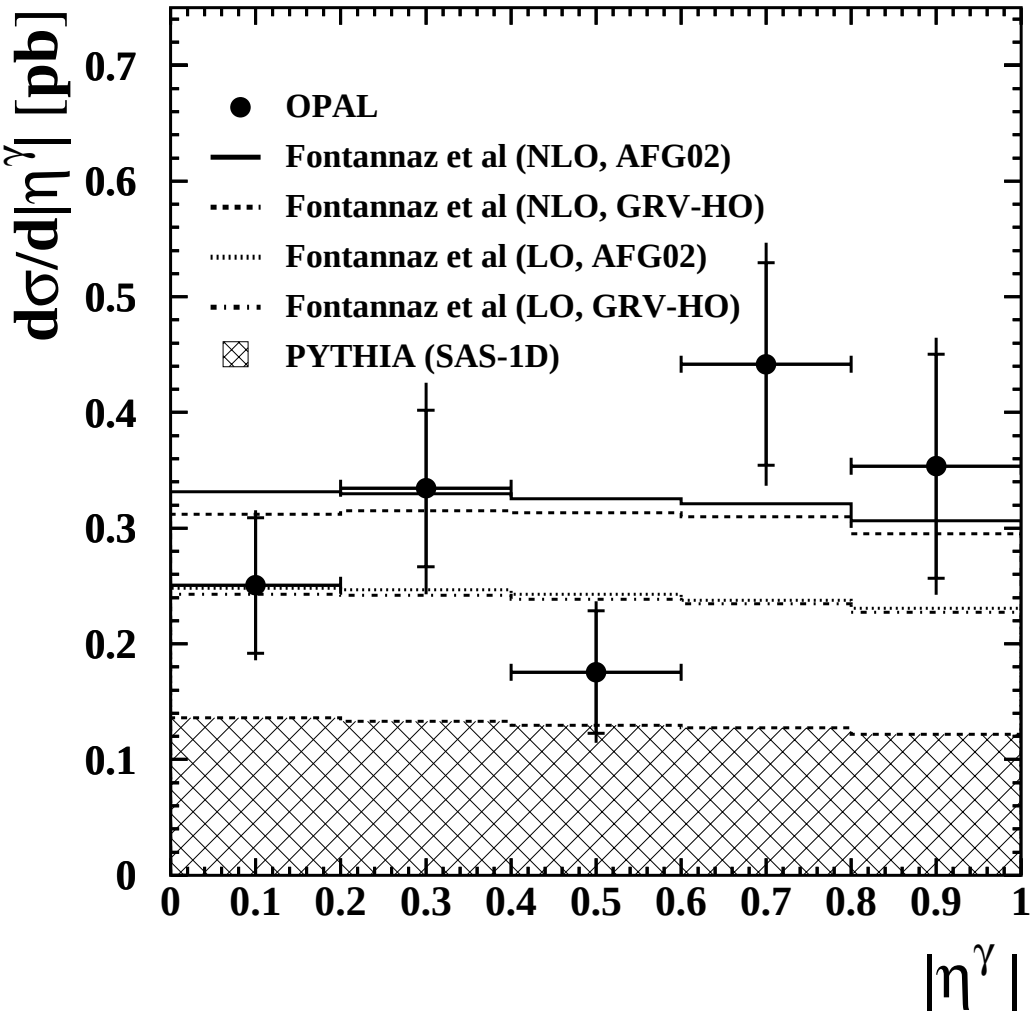


Figure 9: Differential cross-section $\mathrm{d}\sigma/\mathrm{d}|\eta^\gamma|$ for inclusive prompt photon production in the kinematic range $|\eta^\gamma| < 1$ and $p_\mathrm{T}^\gamma > 3.0$ GeV. The points represent data. The inner error bars show the statistical uncertainty and the outer error bars the total uncertainty.

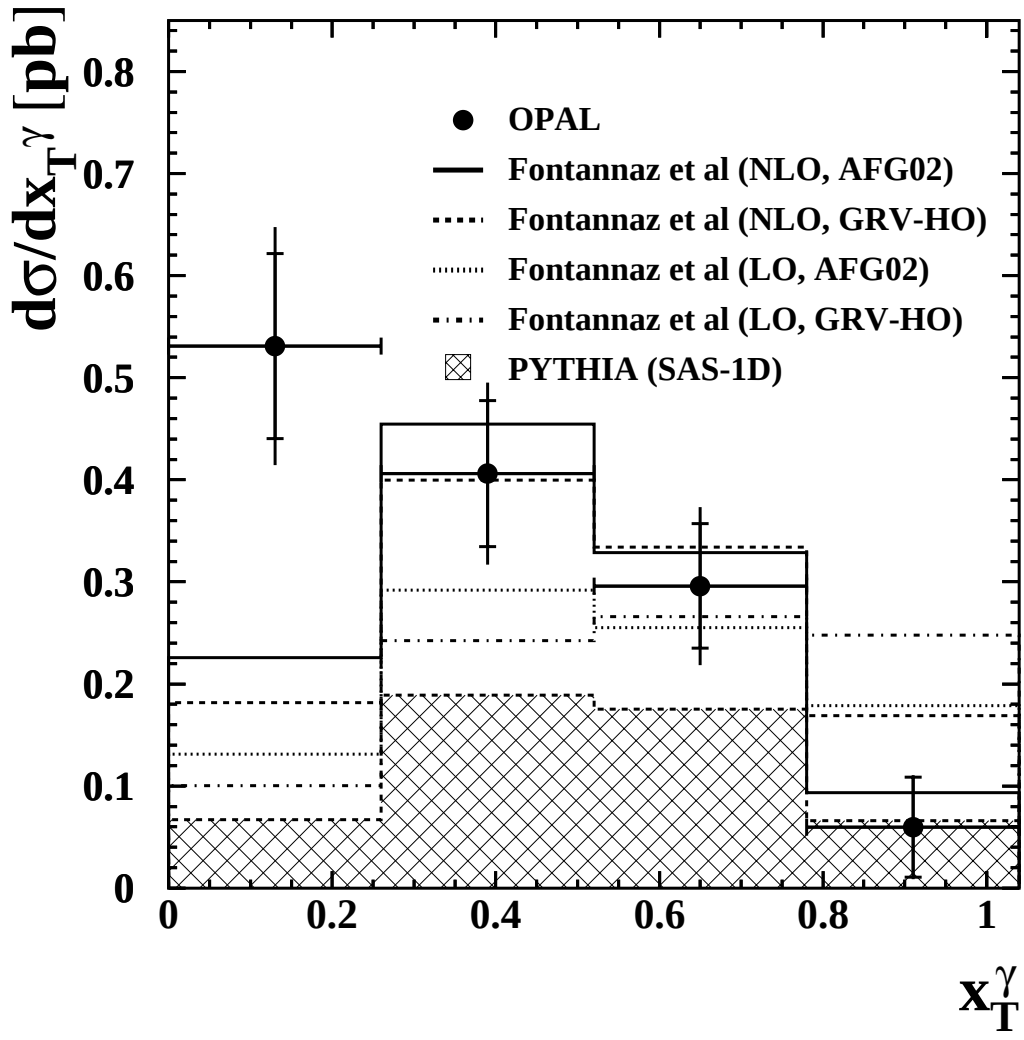


Figure 10: Differential cross-section $\mathrm{d}\sigma/\mathrm{d}x_{\mathrm{T}}^{\gamma}$ for inclusive prompt photon production in the kinematic range $|\eta^{\gamma}| < 1$ and $p_{\mathrm{T}}^{\gamma} > 3.0$ GeV. The points represent the data. The inner error bars show the statistical uncertainty and the outer error bars the total uncertainty.

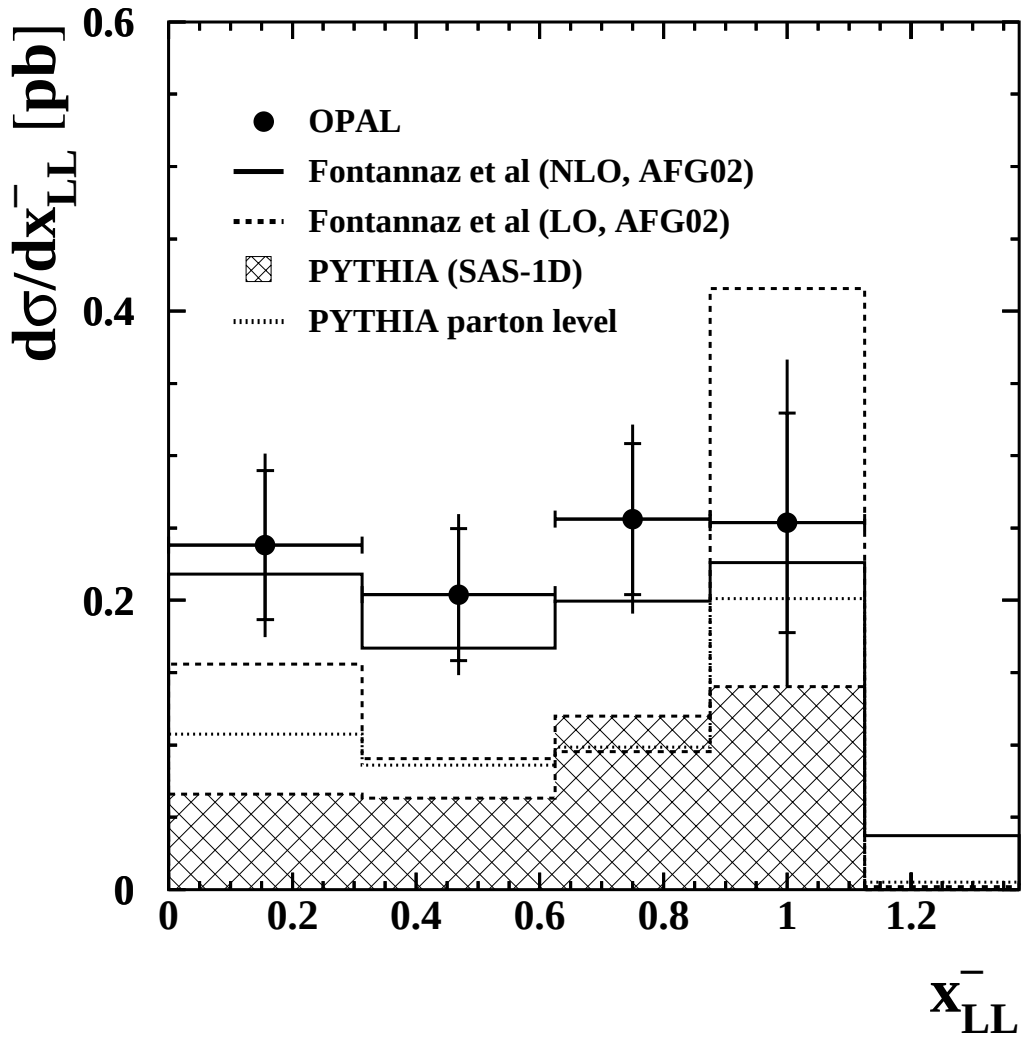


Figure 11: Differential cross-section $\mathrm{d}\sigma/\mathrm{d}x_{\mathrm{LL}}^{-}$ for the production of a prompt photon in association with at least one jet in the kinematic range $|\eta^{\gamma}| < 1$, $p_{\mathrm{T}}^{\gamma} > 3.0$ GeV, $|\eta^{\mathrm{jet}}| < 2$, and $p_{\mathrm{T}}^{\mathrm{jet}} > 2.5$ GeV. The points represent the data. The inner error bars show the statistical uncertainty and the outer error bars the total uncertainty.